The Astrophysical Journal, 799:20 (7pp), 2015 January 20 doi:10.1088/0004-637X/799/1/20
© 2015. The American Astronomical Society. All rights reserved.

FULLY CONVECTIVE MAGNETO-ROTATIONAL TURBULENCE IN LARGE ASPECT-RATIO SHEARING BOXES

G. Bodo[1], F. Cattaneo[2,3], A. Mignone[4], and P. Rossi[1]
[1] INAF, Osservatorio Astronomico di Torino, Strada Osservatorio 20, I-10025 Pino Torinese, Italy; bodo@oato.inaf.it
[2] The Computation Institute, The University of Chicago, 5735 South Ellis Avenue, Chicago, IL 60637, USA
[3] Department of Astronomy and Astrophysics, The University of Chicago, 5640 South Ellis Avenue, Chicago, IL 60637, USA
[4] Dipartimento di Fisica, Univesità di Torino, via Pietro Giuria 1, I-10125 Torino, Italy
Received 2014 January 7; accepted 2014 November 3; published 2015 January 12

ABSTRACT

We present a numerical study of turbulence and dynamo action in stratified shearing boxes with both finite and zero net magnetic flux. We assume that the fluid obeys the perfect gas law and has finite thermal diffusivity. The latter is chosen to be small enough so that vigorous convective states develop. The properties of these convective solutions are analyzed as the aspect ratio of the computational domain is varied and as the value of the mean field is increased. For the cases with zero net flux, we find that a well-defined converged state is obtained for large enough aspect ratios. In the converged state, the dynamo can be extremely efficient and can generate substantial toroidal flux. We identify solutions in which the toroidal field is mostly symmetric about the mid-plane and solutions in which it is mostly anti-symmetric. The symmetric solutions are found to be more efficient at transporting angular momentum and can give rise to a luminosity that is up to an order of magnitude larger than the corresponding value for the anti-symmetric states. In the cases with a finite net flux, the system appears to spend most of the time in the symmetric states.

Key words: accretion, accretion disks – dynamo – magnetohydrodynamics (MHD) – turbulence

1. INTRODUCTION

The turbulence driven by the magneto-rotational instability (MRI) is largely responsible for the enhanced transport of angular momentum in hot accretion disks (Balbus & Hawley 1991). Remarkably, the magnetic fields necessary for the MRI to develop can either be externally imposed or internally generated within the disk. In this latter case, the magneto-rotational turbulence also acts as a dynamo. Consequently, much effort has been devoted to the study of dynamo action within accretion disks (Hawley et al. 1996; Fromang & Papaloizou 2007; Pessah et al. 2007; Käpylä & Korpi 2011; Bodo et al. 2011; Riols et al. 2013). These studies seek to determine which factors control the dynamo processes and under what conditions the dynamo can be sufficiently effective to generate the magnetic fields necessary to account for the inferred accretion rates. Several recent studies have incorporated some form of vertical stratification within the disk and have shown that the operation of the dynamo depends crucially on how the disk is stratified (Davis et al. 2010; Shi et al. 2010; Oishi & Mac Low 2011; Gressel 2010; Guan & Gammie 2011; Simon et al. 2012; Bodo et al. 2012, 2013). The stratification, in turn, depends on the microscopic properties of the material in the disk, such as, for instance, its equation of state or its thermal transport properties. For pressure-dominated, optically thick disks with a perfect gas equation of state, Bodo et al. (2012, henceforth Paper I) have shown that, depending on the efficiency of thermal conduction, two regimes of operation are possible with dramatically different dynamo properties. In particular, if thermal conduction is inefficient, the disk becomes unstable to overturning motions that lead to a vertical structure in which the density is nearly homogeneous across the layer. In this "fully convective" regime, the dynamo appears to be much more efficient—and consequently, so is the angular momentum transport—than in the case in which the thermal conduction is efficient and the disk remains stable to convection. In this latter case and similarly to a disk with an isothermal equation of state, the density decreases rapidly with height.

In Paper I, simple thermal boundary conditions were adopted in which the temperature was fixed on the horizontal boundaries and set to be equal to that of the initial isothermal hydrostatic equilibrium. In a subsequent paper, Bodo et al. (2013, henceforth Paper II) have shown that the fully convective regime and its associated dynamo action persists even when more realistic radiative boundary conditions are applied. In this case, the operating temperature of the disk is no longer "pinned" by the initial value, rather it is determined self-consistently by the balance between energy production and energy losses by radiation. Ultimately, the factor determining whether the disk becomes fully convective or not is the Péclet number—the ratio between thermal relaxation time and the orbital period, say—thus these results establish an interesting relationship between the opacity within the disk and its accretion rate.

Because the convective motions play such a crucial role in determining the vertical structure of the disk and control the dynamo efficiency, it is important that the convection be properly captured by the numerical models. It is well known that the convective efficiency is influenced both by the aspect ratio of the convective domain and by the presence of large-scale magnetic fields. If the aspect ratio is too small, the convective structures might not be able to form with their natural size, thereby affecting the convective transport (Chandrasekhar 1981). Also, the presence of a uniform magnetic field can affect both the morphology and transport property of the convection with possible consequences for the accretion rate (Cattaneo et al. 2003). In Papers I and II, only cases with zero net flux were considered and the aspect ratio was fixed. Its value was modest and chosen so that the exploration of a wide range of parameters remained computationally affordable. We return to these issues in the present work and consider the effects of imposing a net

(vertical) flux threading the layer and of varying the aspect ratio of the computational domain. In both cases, the main objective is to assess how variations in convective planform induced by changes in aspect ratio and by the presence of a uniform magnetic field affect the convective efficiency, the disk structure, and ultimately the accretion rate. Recently, the cases with net magnetic flux have attracted particular interest because of the possibility of driving outflows from their surface layers. The presence of outflows has been shown in isothermal simulations (Lesur et al. 2013; Bai & Stone 2013; Fromang et al. 2013) and critically depends on the choice of boundary conditions. Because we are primarily interested in the convective properties of the interior, we confine our study to cases with small thermal conductivity (large Péclet number) and boundary conditions that do not allow the formation of outflows.

2. FORMULATION

We extend our analysis of fully convective MRI driven turbulence in shearing boxes by considering domains with different aspect ratios and both cases with zero and net magnetic flux. The formulation is similar to those in Papers I and II. We perform three-dimensional numerical simulations of a perfect gas with finite thermal conduction in a shearing box with vertical gravity. The magnetohydrodynamics shearing box equations, including vertical gravity and thermal conduction, can be written in dimensionless form as

$$\frac{\partial \rho}{\partial t} + \nabla \cdot (\rho \mathbf{v}) = 0, \tag{1}$$

$$\frac{\partial \mathbf{v}}{\partial t} + \mathbf{v} \cdot \nabla \mathbf{v} + 2\hat{\mathbf{e}}_z \times \mathbf{v} = \frac{\mathbf{B} \cdot \nabla \mathbf{B}}{4\pi\rho} - \frac{1}{\rho}\nabla P_T + 3x\hat{\mathbf{e}}_x - z\hat{\mathbf{e}}_z, \tag{2}$$

$$\frac{\partial \mathbf{B}}{\partial t} - \nabla \times (\mathbf{v} \times \mathbf{B}) = 0, \tag{3}$$

$$\frac{\partial E}{\partial t} + \nabla \cdot \left[(E + P_T)\mathbf{v} - \frac{(\mathbf{v} \cdot \mathbf{B})\mathbf{B}}{4\pi} - \frac{\gamma}{\gamma - 1}\rho \frac{1}{\mu}\frac{1}{P_e}\nabla T \right] = 0, \tag{4}$$

and

$$P = \frac{1}{\mu}\rho T, \tag{5}$$

where $\mathbf{B}$, $\mathbf{v}$, ρ, and P denote, respectively, the magnetic field intensity, the velocity, the density, and the thermal pressure; E is the total energy density, P_T is the total (thermal plus magnetic) pressure, μ is the mean molecular weight, and γ is the ratio of specific heats. In Equation (5), we have absorbed the perfect gas constant R in the definition of the temperature. The dimensionless form has been obtained by choosing the half thickness of the disk D as the unit of length, the inverse of the rotation rate $1/\Omega$ as the unit of time, and the average density $\rho_{\rm av}$ as the unit of density. With these choices, the unit of temperature is $\Omega^2 D^2$; the unit of magnetic field intensity is $\sqrt{\rho_{\rm av}\Omega^2 D^2}$; and the unit of pressure, energy density, Maxwell, and Reynolds stresses is $\rho_{\rm av}\Omega^2 D^2$. The equations depend only on one nondimensional number—the Péclet number, defined as

$$P_e = \frac{\Omega D^2}{\kappa}, \tag{6}$$

where κ is the thermal diffusivity that we assume to be constant. Since we are primarily interested in the convective regimes in which κ only plays a role in the thermal boundary layers, this assumption is not too restrictive. An additional nondimensional number is introduced by the vertical thermal radiative boundary conditions that are given by

$$\frac{\rho}{P_e}\frac{dT}{dz} \pm \Sigma T^4 = 0 \qquad \text{at} \qquad z = \pm 1. \tag{7}$$

The radiation parameter Σ, up to a factor of $2(\gamma - 1)/\gamma$, is the ratio of two energy fluxes: the radiative flux of a blackbody at temperature T—measured in units of $\Omega^2 D^2$—divided by the kinetic energy flux of a fluid of density $\rho_{\rm av}$ moving at the isothermal sound speed. Substitution of the dimensional quantities in Equation (7) gives

$$\Sigma = \frac{\gamma - 1}{\gamma}\frac{\sigma \Omega^5 D^5 \mu}{R^4 \rho_{\rm av}}, \tag{8}$$

where σ is the Stefan-Boltzmann constant. We notice that this definition is slightly different from that adopted in Paper II. The reason is that in Papers I and II, we were interested in making contact with the isothermal cases and thus we chose a slightly different definition and nondimensionalization than the one adopted here.

Additionally, as it is customary in shearing box simulations, we assume periodic boundary conditions in the y-direction and shear periodic conditions in the x-direction. In the vertical direction, in addition to the radiative thermal boundary condition, we assume that the upper and lower boundaries ($z = \pm 1$) are impenetrable and stress free, giving $v_z = 0$, $\partial v_x/\partial z = \partial v_y/\partial z = 0$, and also that the magnetic field is purely vertical, giving $\partial B_z/\partial z = 0$, $B_x = B_y = 0$. Additionally, we assume that the boundaries are in hydrostatic balance. We briefly comment on this particular choice of boundary conditions here; for a lengthier discussion, we refer the reader to Paper II. Impenetrable, stress-free boundary conditions such as the ones we adopt here are commonly used in numerical studies of convective layers. They represent an idealization of a region in which the collisional thermal transport properties of the plasma change dramatically; for instance, a transition from an optically thick to an optically thin medium. In general, a realistic treatment would require that both regions be taken into account and simulated concurrently. Though possible, this approach is generally very expensive since the transition introduces strong numerical stiffness into the equations. If one is primarily interested in the interior solution, as we are in the present paper, replacing the transition layer with a stress-free impenetrable boundary is not unreasonable. We should mention, however, the recent work of Gressel (2013) in which two cases are compared—one with impenetrable stress-free boundaries and one with open boundaries and homogeneous thermal diffusivity. Not surprisingly, the convection is greatly suppressed in the open boundary case. As we noted in Paper II, this is not a very meaningful comparison. A sensible study should contrast different cases in which the transition from low to high thermal conductivity occurs more or less abruptly. Actually, the results of such a study have recently been presented by Hirose et al. (2014), who incorporate a realistic treatment of opacity variations at temperatures around the hydrogen ionization range. The results show that, indeed, convection sets in the dense opaque regions near the disk center exactly as anticipated by the arguments based on the idealized boundary conditions.

We start our simulations from a state with a uniform shear flow, $\mathbf{v} = -3/2x\hat{\mathbf{e}}_y$, and density and pressure distributions that

Table 1
Aspect Ratios and Number of Computational Cells Used in the Simulations with Zero Net Flux

Case	A_x	A_y	N_x	N_y
A	0.25	0.75	32	96
B	1	3	128	384
C	2	3	256	384
D	4	3	512	384

satisfy vertical hydrostatic balance with constant temperature. The initial density has a Gaussian profile given by

$$\rho = \frac{1}{H\,\mathrm{erf}(1/H)}\exp(-z^2/H^2), \tag{9}$$

where H is the isothermal scale height measured in units of D and erf is the error function. Equation (9) satisfies the normalization condition

$$\frac{1}{2}\int_{-1}^{1}\rho dz = 1. \tag{10}$$

For numerical reasons (see Paper II), we do not apply the radiative boundary conditions from the beginning of the simulations; instead, we proceed in two phases. In the first phase, we keep the temperature at the boundaries fixed at the initial value until the system reaches a stationary state (typically the first phase lasts 1000 time units), then we start the second phase by imposing radiative boundary conditions and follow the evolution for a sufficiently long time to have reasonable statistics. Typically this is achieved in another 1000 time units. We note that the form of initial conditions introduces the additional parameter H. However, the final convective state is independent of this choice. Furthermore, for large Péclet numbers, the solution in the convective interior becomes independent of the Péclet number, thus in the convective regime, the final steady state depends only on Σ.

The size of the computational domain is given by $2[A_x, A_y, 1]$. All the simulations were carried out with the PLUTO code (Mignone et al. 2007) with a second-order accurate linear reconstruction, HLLD Riemann solver, an explicit treatment of thermal conduction, and a uniform resolution of 64 grid points per unit length.

3. RESULTS

We perform two series of simulations: one with zero mean magnetic flux and different values of the aspect ratios A_x and A_y and one with a net magnetic flux threading the box and with different values of the magnetic field strength. We consider only fully convective solutions and fix the Péclet number at 1000 and the mean molecular weight $\mu = 0.5$ (fully ionized hydrogen). We choose $\Sigma = 4$ for all the simulations; this is the value appropriate to the continuations of solutions presented in Paper II. Variations of the solutions with Σ will be considered elsewhere.

Table 1 summarizes the values of the aspect ratios A_x and A_y and the number of grid points N_x and N_y used in the first set of simulations with no net flux. Each solution was integrated with the radiative boundary conditions for 1000 time units except for case D, which was integrated for twice as long.

The initial magnetic field was of the form

$$\mathbf{B} = B_0 \sin(2\pi x)\,\hat{\mathbf{e}}_z, \tag{11}$$

Table 2
Magnetic Field Strength, Plasma β at the Midplane, Domain Size, and Number of Computational Cells Used in the Simulations with Net Magnetic Flux

Case	B_0	β	A_x	A_y	N_x	N_y
E	0.02	1250	4	3	512	384
F	0.04	312	4	3	512	384
G	0.1	50	4	3	512	384

where B_0 corresponds to a ratio of thermal to magnetic pressure of 1600.

The second set of simulations was carried out with the largest domain size and with a net vertical magnetic flux threading the box. The initial magnetic field was given by

$$\mathbf{B} = B_0\hat{\mathbf{e}}_z, \tag{12}$$

where the values of B_0 are specified in Table 2. The choice of computational domain with the largest aspect ratio for the cases with net flux was dictated by the fact that in smaller boxes the solutions are dominated by spurious channel flows (Bodo et al. 2008). When stratification is present, these flows can lead to strong numerical instabilities (Miller & Stone 2000). The length of the simulations with radiative boundary conditions was 1000 time units for all three cases.

3.1. Convergence for the Cases with Zero Flux

The first series of simulations was aimed at investigating how the properties of the turbulent state depend on the values of the aspect ratios and whether they converge as the latter are increased. For case A, we choose values of the aspect ratios similar to those used in Papers I and II to facilitate a comparison. More precisely, here we have $A_x = 0.25$ and $A_y = 0.75$, while in Papers I and II, we had $A_x = 0.167$ and $A_y = 0.75$. In all the other cases, we vary A_x, keeping $A_y = 3$.

It is helpful to introduce some notation: if f is a generic function of space and time, we indicate a volume average by $\bar{f}$, an average over horizontal planes by $\tilde{f}$, and a time average by $\langle f\rangle$. For comparison purposes, in this subsection, in order to have the same time interval for all the cases, we make use of the second half of the simulation in case D.

Figure 1 shows the vertical profile of $\langle\tilde{T}(z)\rangle$ for the different cases. It is immediately obvious that the case with the smallest aspect ratio (case A) is way off relative to the other cases. As we move to larger aspect ratios, the overall temperature increases and the profile becomes flatter. Also, there is a clear indication that the curves converge to an asymptotic profile as A_x becomes large. The corresponding density profiles are flat in all four cases. The Maxwell stresses also show a sharp increase between case A and the other three cases. This is illustrated in Figure 2, where the volume-averaged Maxwell stresses are shown as a function of time. The differences between cases C and D is relatively small, again indicating an approach to a converged state.

The differences in angular momentum transport, as measured by the Maxwell stresses, can be related to differences in the efficiency of the dynamo processes. One of the distinctive features of dynamo action in the convective regime is that it can lead to the generation of a substantial amount of toroidal flux. Thus the production of toroidal flux can be used as a measure of dynamo efficiency. Figure 3 shows the space and time distribution of the azimuthal component of the horizontally averaged magnetic field $\tilde{B}_y(z,t)$ for the same three cases shown

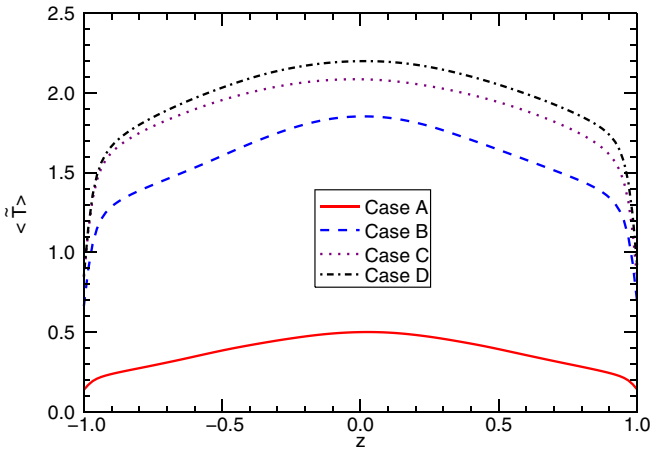


Figure 1. Horizontally and time-averaged profiles of the temperature as functions of z for the cases A–D with zero net flux and different aspect ratios. The corresponding averaged surface heat fluxes for cases A–D are, respectively, 0.012, 0.18, 0.26, and 0.29.

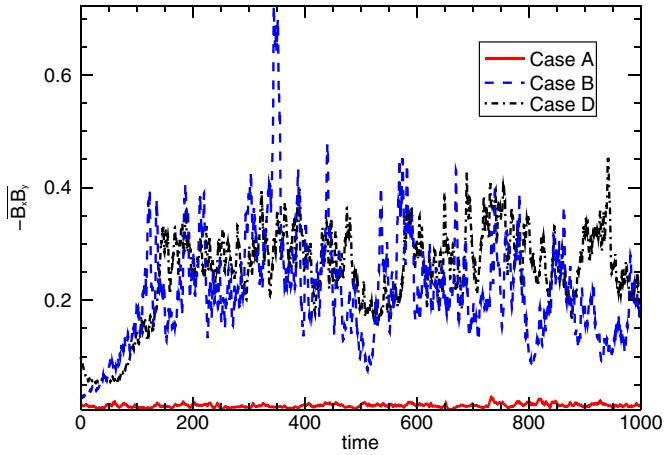


Figure 2. Time histories of the Maxwell stresses averaged over the computational box for the cases A, B, and D with zero net flux and different aspect ratios. The time history for case D covers the second half of the simulation, the full time history for this case is shown in Figure 5.

in Figure 2. In case A (top panel), the average $\tilde{B}_y$ shows changes in sign over small intervals both in time and in the vertical spatial direction. The episodes in which the entire layer becomes magnetized are of short duration. With the increase in aspect ratio in case B (middle panel), we observe the emergence of two kinds of dominant z distribution: a symmetric one in which $\tilde{B}_y$ has the same sign, positive or negative, over the whole vertical extent and an anti-symmetric one in which $\tilde{B}_y$ changes sign. The system switches between these states with an average persistence time in any one state of about 100 time units. In addition, there is a substantial increase in the overall amplitude of the generated field with respect to case A. In the bottom panel, corresponding to case D, the magnetic field strength is similar to case B, but the system locks into a symmetric state and keeps it for about 1000 time units. It can be argued that a large-scale dynamo appears to be at work in all cases; however, its efficiency depends on the aspect ratio.

The reason for the large differences between case A and the other three cases is perhaps most apparent in Figure 4, where we plot the temperature distribution on a horizontal plane at the top of the computational box for case D. The figure shows

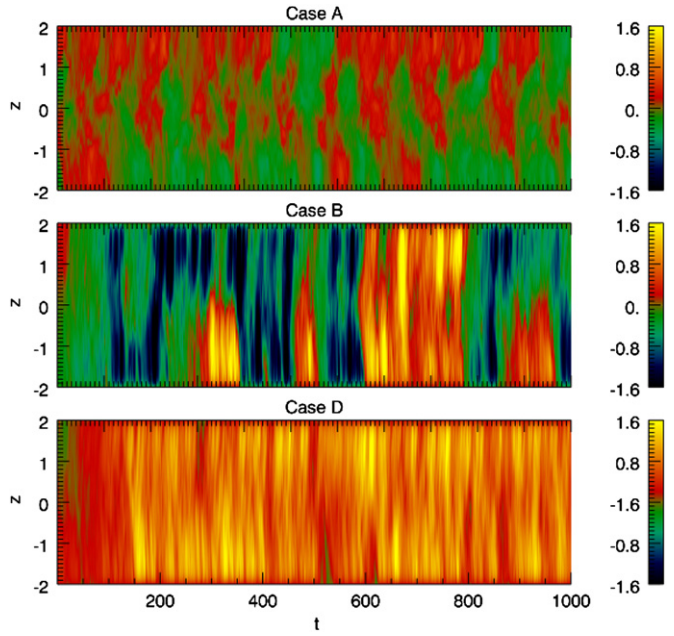


Figure 3. Space–time diagrams of the average azimuthal field. The horizontally averaged value of B_y is plotted as a function of z and t. The three panels refer to cases A, B, and D with zero net flux and different aspect ratios. The diagram for case D covers the second half of the simulation, the diagram for the full simulation length is shown in Figure 6. The corresponding values of the plasma β are $\gtrsim 1$.

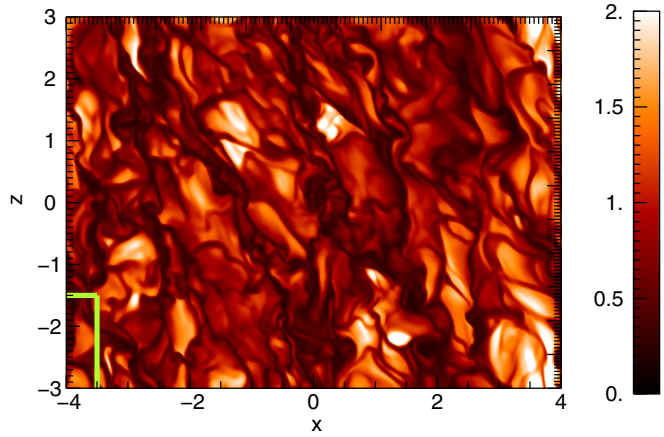


Figure 4. Typical temperature planform at the upper boundary of the computational box for case D with zero net flux and the largest aspect ratio. The green rectangle in the lower left corner of the figure shows the extent of the computational grid for case A.

that the convective pattern consists of a network of cells with wide warmer upflows and concentrated colder downflows. The pattern evolves rapidly on a timescale of approximately 10 time units and shows an overall structuring along diagonal lines. The green rectangle in the lower left corner of the figure shows the extent of the computational grid for case A. Although it is difficult to assign a precise measure for the size of the convective cells, it is clear that the green box is too small adequately to capture the spatial structure of the convection.

3.2. The Converged Solution with Zero Net Flux

In the previous subsection, we presented evidence that the properties of the turbulent state appear to converge as the aspect ratio is increased. Here we look at case D as good representation

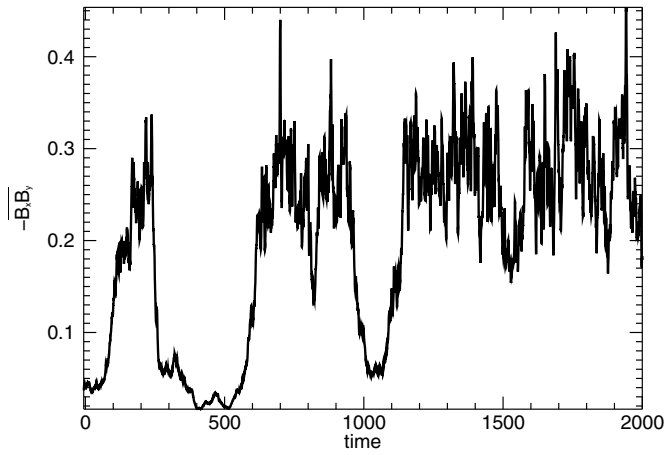


Figure 5. Time history of the Maxwell stresses averaged over the computational box for case D. The time history covers the full simulation length of 2000 time units.

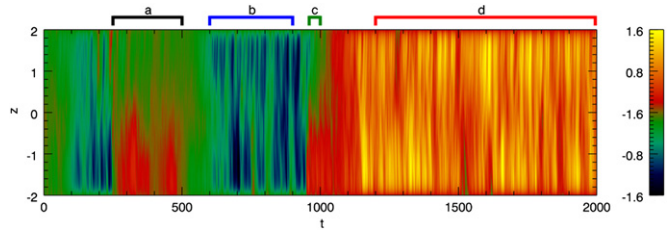


Figure 6. Space–time diagram of the average azimuthal field for case D. The horizontally averaged value of B_y is plotted as a function of z and t. The diagram covers the full simulation length of 2000 time units. Above the diagrams we have marked four time intervals, denoted by the letters a, b, c, and d, during which we have alternatively low and high states. The time-averaged vertical profiles of azimuthal field shown in Figure 7 refer to these four time intervals.

of the eventual asymptotic state. As remarked earlier, we evolved this simulation for a longer time interval than the other cases; in Figure 5, we plot the volume-averaged Maxwell stresses as a function of time for the entire length of the simulation. The figure clearly shows the existence of two states with higher and lower values of the stresses with an evident predominance of the higher state.

If we compare Figure 5 with Figure 6, in which we display the space–time distribution of the azimuthal component of the horizontally averaged magnetic field $\tilde{B}_y(z, t)$, it appears that the episodes with higher and lower transport efficiency correspond, respectively, to the symmetric and anti-symmetric states introduced earlier. Also, we note that the anti-symmetric state may mark the transition between two symmetric states of opposite polarity.

The symmetric and anti-symmetric nature of the two solutions is made clearer in Figure 7, where we plot $\langle \tilde{B}_y(z) \rangle$ as a function of z. The different curves correspond to the different time intervals on which the averages are taken; the corresponding time intervals are marked on top of Figure 6. The two symmetric states have opposite polarity and similar field strength, while the second of the two anti-symmetric states (curve c) is somewhat stronger than the first. The total length of time in which the solution is anti-symmetric is about one-fourth of the length of time in which it is symmetric; however, to obtain a statistically meaningful estimate of this fraction, a much longer simulation is needed. The differences in transport efficiency between the symmetric and anti-symmetric states also manifest themselves

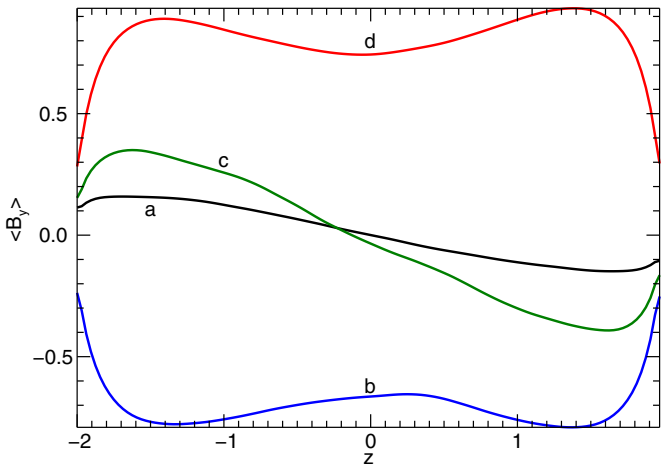


Figure 7. Vertical profile of the time-averaged azimuthal field as functions of z. The four curves refer to the four time intervals—a, b, c, and d—marked in Figure 6, for which we have alternatively low and high states.

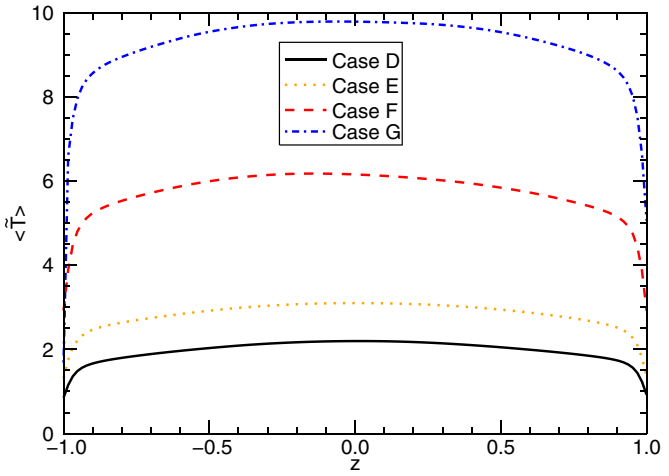


Figure 8. Horizontally and time-averaged profiles of the temperature as functions of z for the cases E–G with net magnetic flux and different initial vertical field strengths. For comparison, we also show case D with zero net flux and the same aspect ratio.

in changes in luminosity that almost exactly track the changes in the Maxwell stresses and can vary up to one order of magnitude.

3.3. The Cases with Finite Net Flux

Having established the properties of the turbulent state in the zero flux case, characterized by the presence of vigorous convective motions and by an efficient large-scale dynamo action, we may now turn to cases with net magnetic field threading the box and ask if and how the presence of a net flux changes the properties of the solutions and how the efficiency of angular momentum transport scales with the value of the magnetic flux.

In Figure 8, we compare the vertical distribution of $\langle \tilde{T}(z) \rangle$ for case D (zero flux, black solid curve) with those of cases E (orange dotted curve), F (red dashed curve), and G (blue dot–dashed curve) with increasing magnetic flux. The shapes of the distributions are quite similar but the temperature values show a small increase in case E and more marked variations for cases F and G. In a similar way, the volume-averaged Maxwell stresses that we plot as a function of time in Figure 9, are slightly higher in case E and much higher for cases F and G.

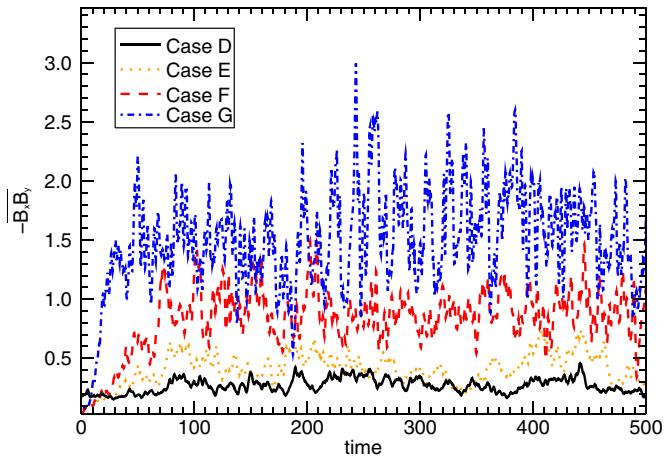


Figure 9. Time histories of the Maxwell stresses averaged over the computational box for the cases E–G with net magnetic flux and different initial vertical field strengths. For comparison, we also show case D with zero net flux and the same aspect ratio.

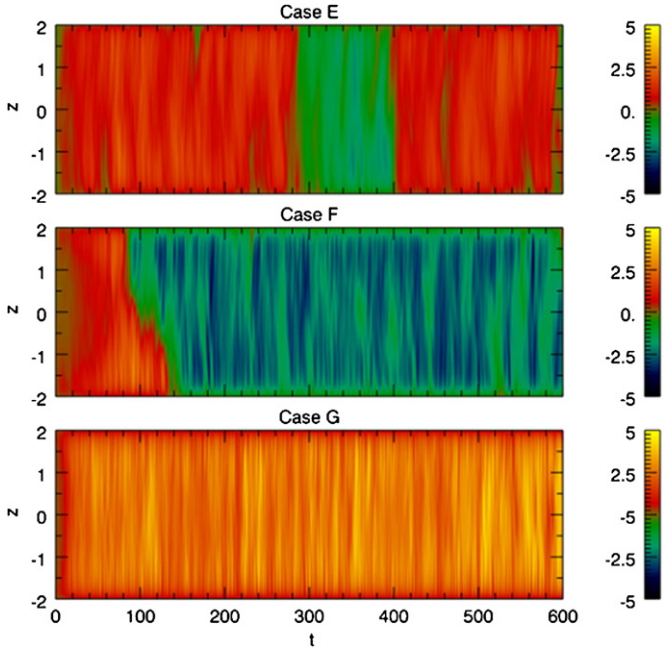


Figure 10. Space–time diagrams of the average azimuthal field. The horizontally averaged value of B_y is plotted as a function of z and t. The three panels refer to cases E–G with net magnetic flux and different initial vertical field strengths. The corresponding values of the plasma β are $\lesssim 1$.

The space–time distributions of $\tilde{B}_y(z)$ for cases E–G are shown in Figure 10. Again we observe that the entire layer is magnetized with sporadic inversions of sign and sometimes at the transition, we observe the appearance of the anti-symmetric state. The strength of $\tilde{B}_y$ increases with the value of the magnetic flux. The corresponding changes in Maxwell stresses are summarized in Figure 11, where the horizontal line correspond to the stresses for case D and we have also indicated the value of B_0 necessary to stabilize the MRI. If we assume that the stresses behave linearly with B_0 near the origin, the intercept with the red line gives a critical value $B_{\rm min}$ of the mean field, below which it makes no difference whether it is present or not. For the system under consideration, $B_{\rm min} \approx 0.02$. To get some feeling for the magnitude of this field strength, we note that the associated wavelength of maximum growth rate in linear theory

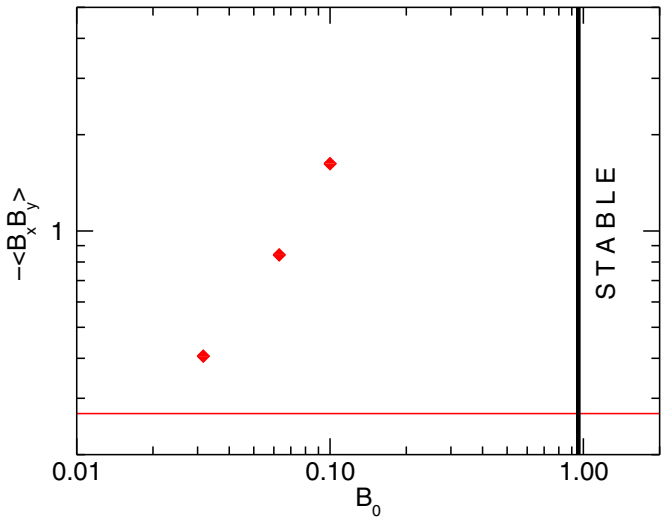


Figure 11. Box and time-averaged values of the Maxwell stresses for cases E–G as a function of the initial vertical field strength B_0. The horizontal line corresponds to the average stress value for case D with zero net flux in the high state. The vertical line shows the linear stability boundary for a state with constant density.

is approximately $1/20$ of the vertical domain size. By contrast, the corresponding quantity for case G is close to $1/3$.

4. CONCLUSIONS

We have analyzed the solutions of the stratified shearing box equations in the convective regime—large Péclet number—as the aspect ratio of the computational domain is varied. We find that for shearing boxes that are about twice as wide as they are tall (or wider) the solution rapidly approaches a "converged" state with a well-defined temperature profile that depends only on the radiation parameter Σ. Smaller boxes are unable adequately to contain the natural convective pattern with the result that the convective efficiency is reduced and the solution operates at a correspondingly lower temperature. The striking characteristic of convective MRI driven turbulence is that it can drive an extremely effective large-scale dynamo capable of generating substantial amounts of toroidal flux. The dynamo itself appears to be similar to that presented in Käpylä & Korpi (2011). It is likely that the role of the convection is not so much to drive the dynamo itself, but rather to homogenize the density, thereby producing a more suitable environment for the dynamo to work. Two broad classes of dynamo solutions can be identified—the ones in which the toroidal flux is symmetric about the mid-plane and the others in which it is anti-symmetric. The symmetric solutions have higher Maxwell stresses and correspondingly higher luminosity. The system appears to swap between these states randomly but typically spend more time in the symmetric, higher-efficiency solutions. The amount of time spent in the symmetric state increases if a net (vertical) magnetic flux is present as does the amplitude of the Maxwell stresses, provided the strength of the mean magnetic field is much less than the critical value needed to stabilize the MRI.

It should be noted that in the present paper, we have often remarked about the efficiency of various solutions but have resisted the temptation to measure it by the parameter α (Shakura & Sunyaev 1973). This was deliberate and it should, to some extent, be justified. In the original formulation by Shakura & Sunyaev (1973), a transport coefficient, namely the effective viscosity was defined in terms of a characteristic length, the

disk thickness, and a characteristic velocity, α times the sound speed. For an isothermal gas, it is customary to replace the disk thickness with the pressure scale height, which in turn is related to the isothermal sound speed, thereby giving a definition of α in terms of the ratio between the stresses and the temperature. This makes perfect sense for an isothermal gas in which the temperature is prescribed. Here, on the other hand, the temperature is determined self-consistently by the solution of the shearing box equations. Nevertheless, we can still ask what kind of values of α are obtained. If we revert to the original formulation in terms of the disk half thickness and recalling that in our units the latter is unity, a definition of α can be obtained by

$$\alpha = \frac{-\langle \overline{B_x B_y} \rangle}{\sqrt{T_{\max}}}, \tag{13}$$

where $T_{\max}$ is the maximum of the temperature and we have neglected the contributions from the Reynolds stresses, which are typically small. A more accurate choice would be to use the average temperature in the denominator, however, since the temperature profile is so flat anyway, definition (Equation (13)) gives a pretty tight lower bound. For cases D–G, the values of α are 0.18, 0.25, 0.35, 0.5, respectively. It should be noted that the difference in α between cased D and G is a factor of 2.8 while their luminosities differ by a factor of 5. Somehow, one feels that the luminosity should be a better measure of transport efficiency, since ultimately it is the value directly related to the accretion rate.

This raises an interesting question: all other things being the same, does a disk with an isothermal equation of state accrete faster or slower than a corresponding convective disk with a perfect gas equation of state? The problem is to decide under what conditions "all other things are the same." Let us restrict our discussion to shearing boxes, and let us assume that we consider computational domains large enough that we obtain converged solutions in terms of the aspect ratios. The isothermal cases are then defined by a single parameter n_H—the number of scale heights per unit length. The perfect gas cases are instead defined by two parameters, the Péclet number P_e and the radiation parameter Σ. The problem is that the radiation parameter is related to the thermal boundary conditions that are absent in the isothermal cases. However, for any Σ, a convective solution can be transformed into a conductive one by decreasing the Péclet number until the solution approaches an isothermal one. If this procedure were repeated for all values of Σ, it would establish a relationship—hopefully a single-valued one—between n_H and Σ, thereby allowing a direct comparison between isothermal and perfect gas solutions. Having said that, we should note that for all the cases that have been studied, the efficiency, measured in terms of the luminosity, say, always increases when the Péclet number is increased and the solution becomes convective. Thus one concludes that a convective disk is always more luminous than a corresponding isothermal one according to the procedure outlined above. Interestingly, the reason for the higher efficiency is not because the convection in itself gives rise to a higher transport of angular momentum, but rather because the convection allows a much more efficient dynamo to operate that generates a strong, coherent toroidal magnetic field that gives rise to a higher angular momentum transport by Maxwell stresses.

This work was supported in part by the National Science Foundation sponsored Center for Magnetic Self Organization at the University of Chicago. G.B., A.M., and P.R. acknowledge support by INAF through an INAF–PRIN grant. We acknowledge that the results in this paper have been achieved using the PRACE Research Infrastructure resource JUQUEEN based in Germany at the Jülich Supercomputing Center.

REFERENCES

Bai, X.-N., & Stone, J. M. 2013, ApJ, 767, 30
Balbus, S. A., & Hawley, J. F. 1991, ApJ, 376, 214
Bodo, G., Cattaneo, F., Ferrari, A., Mignone, A., & Rossi, P. 2011, ApJ, 739, 82
Bodo, G., Cattaneo, F., Mignone, A., & Rossi, P. 2012, ApJ, 761, 116
Bodo, G., Cattaneo, F., Mignone, A., & Rossi, P. 2013, ApJL, 771, L23
Bodo, G., Mignone, A., Cattaneo, F., Rossi, P., & Ferrari, A. 2008, A&A, 487, 1
Cattaneo, F., Emonet, T., & Weiss, N. 2003, ApJ, 588, 1183
Chandrasekhar, S. 1981, Hydrodynamic and Hydromagnetic Stability (Dover Classics of Science and Mathematics; New York: Dover) (cop. 1961)
Davis, S. W., Stone, J. M., & Pessah, M. E. 2010, ApJ, 713, 52
Fromang, S., Latter, H., Lesur, G., & Ogilvie, G. I. 2013, A&A, 552, A71
Fromang, S., & Papaloizou, J. 2007, A&A, 476, 1113
Gressel, O. 2010, MNRAS, 405, 41
Gressel, O. 2013, ApJ, 770, 100
Guan, X., & Gammie, C. F. 2011, ApJ, 728, 130
Hawley, J. F., Gammie, C. F., & Balbus, S. A. 1996, ApJ, 464, 690
Hirose, S., Blaes, O., Krolik, J. H., Coleman, M. S. B., & Sano, T. 2014, ApJ, 787, 1
Käpylä, P. J., & Korpi, M. J. 2011, MNRAS, 413, 901
Lesur, G., Ferreira, J., & Ogilvie, G. I. 2013, A&A, 550, A61
Mignone, A., Bodo, G., Massaglia, S., et al. 2007, ApJS, 170, 228
Miller, K. A., & Stone, J. M. 2000, ApJ, 534, 398
Oishi, J. S., & Mac Low, M.-M. 2011, ApJ, 740, 18
Pessah, M. E., Chan, C., & Psaltis, D. 2007, ApJL, 668, L51
Riols, A., Rincon, F., Cossu, C., et al. 2013, JFM, 731, 1
Shakura, N. I., & Sunyaev, R. A. 1973, A&A, 24, 337
Shi, J., Krolik, J. H., & Hirose, S. 2010, ApJ, 708, 1716
Simon, J. B., Beckwith, K., & Armitage, P. J. 2012, MNRAS, 422, 2685